Small-Angle Oblique-Incidence Infrared Reflection in Polar Materials: I. Model Approach

Noritaka KURODA* and Yoshinori TABATA[1]

Free Laboratory for Materials Technology, Shimizunuma 2-10-11, Miyagino-ku, Sendai 983-0845, Japan

[1]*Faculty of Pharmaceutical Sciences, Hokuriku University, Kanazawa 920-1181, Japan*

(Received August 14, 2009; accepted November 19, 2009; published)

Nearly normal off-axis infrared reflection due to polar optical phonons has been examined numerically for cubic and uniaxial crystals. Even at a small angle of incidence, Brewster's law causes null reflection to the *p*-polarized light at frequencies just above LO modes, since the dielectric function monotonically increases from zero with increasing frequency above an LO mode. The total reflection due to Snell's law may also take place in *s*- and *p*-polarizations. These effects give rise to steep minima and maxima, depending on the orientation and phonon structure of the crystal examined, in the reflection spectrum around LO modes. Although the structures are suppressed strongly by damping, they may become sufficiently intense to be experimentally observed in real bulk crystals if the angle of incidence is elevated up to approximately 10°. On the basis of these findings, we propose that small-angle oblique-incidence reflectometry is a reliable method of characterizing optical phonons in polar materials.

KEYWORDS: infrared ellipsometry, small-angle oblique-incidence reflection, *s*-polarization, *p*-polarization, Brewster's law, Snell's law, polar optical lattice vibration, LO phonon

*E-mail address: kurodaflmt@ac.auone-net.jp

1. Introduction

Any material exhibits different responses to the radiation between *s*- and *p*-polarizations if the radiation is obliquely incident to the surface of the material, where *s* and *p* signify the directions of the linear polarization of the electric field of radiation that are perpendicular and parallel to the plane of incidence, respectively. The crystal optics of isotropic materials for these linearly polarized radiations has been described by Born and Wolf. [1)] A study on the reflection and transmission of light in uniaxial crystals has been conducted by Mosteller and Wooten.[2)] Decius et al. have examined the *p*-polarized oblique-incidence infrared reflection in anisotropic crystals with a symmetry as high as or higher than orthorhombic,[3)] showing that if the lattice vibration is sufficiently anisotropic, a prominent reflection may appear in the *p*-spectrum at frequencies above a longitudinal optical (LO) mode polarized perpendicular to the surface of the crystal. The work of Decius et al. has motivated Piro[4)] to carry out a general theoretical analysis of the reflection and transmission of absorbing anisotropic crystal plates.

Berreman has studied the infrared transmission and reflection of thin LiF films deposited on a collodion film,[5)] demonstrating that, for *s*-polarized radiation, there is only one transmission minimum at the resonance frequency of the transverse optical (TO) mode of lattice vibration, while, for *p*-polarized radiation, transmission minima are observed at both the resonance frequencies of the TO and LO modes. Berreman has also shown that a significant attenuation of light occurs due to the excitation of LO phonons if *p*-polarized infrared light is incident obliquely on thin films of ionic crystals deposited on a metallic substrate. Sciacca et al. [6)] have applied this Berreman technique to the examination of phonon structures in various compound semiconductors.

Since the responses of a material to *s*- and *p*-polarized radiations are independent of each other, they enable us to evaluate the real and imaginary parts of the dielectric function without the aid of the Kramers-Kronig relations, which require an infinitely wide range of either reflection or transmission spectrum to evaluate the complex dielectric function. Let the amplitude reflectivities of *s*- and *p*-polarizations be r_s and r_p, respectively. The larger the angle of incidence, the larger the deviation in the ratio r_p/r_s from unity, and therefore the higher the accuracy of the complex dielectric function derived. Consequently, the oblique incidence reflection method using a high angle of incidence of 30–80° has been applied to a variety of materials successfully. A method of obtaining the dielectric function from the complex r_p/r_s measured at an angle of incidence of 60–80° is called spectroscopic ellipsometry.[7, 8)]

In this paper we are concerned with the off-axis infrared reflection in bulk crystals at an

angle of incidence of approximately 10°, which is much smaller than the angles employed in spectroscopic ellipsometry. Practically, this situation has been treated as normal incidence, and therefore the influence of oblique incidence has so far been disregarded in countless studies on the optical reflectometry of solids. However, since the dielectric function of the lattice in a polar crystal monotonically increases with increasing frequency above a TO phonon, changing its sign from negative to positive at an LO phonon, Brewster's law[1)] should hold even for such a small angle of incidence to cause null reflection to *p*-polarized radiation at a frequency just above the LO phonon. For the same reason, one may expect that the total reflection due to Snell's law takes place in *s*- and *p*-polarizations in the close vicinity of Brewster's null reflection. As a result, there should appear steep minima and maxima in the reflection spectrum around an LO phonon. In order to examine the validity of this conjecture, we carry out numerical calculations of small-angle oblique-incidence reflection spectra in model crystals of cubic and uniaxial materials. Details of the approach and the calculated spectra are described in §2. The results are discussed in §3 and summarized in §4. In separate papers, we will report experimental studies on the application of this method, of which a preliminary report has been presented elsewhere[9)].

2. Oblique-Incidence Reflection from Principal Faces of Crystals

The properties of the optical reflection of bulk crystals depend on crystallographic orientation. We consider the reflection from the principal face of a crystal oriented as shown in Fig. 1, where the axes of crystal symmetry are all parallel to the axes x_j's of j = 1, 2, and 3 of the Cartesian coordinates of the laboratory system. Let the principal dielectric functions be $\varepsilon_{(j)}$'s and suppose that the plane of incidence stands vertically on this crystal face along the x_2 direction and the infrared light is incident in this plane at an angle of θ. The reflectivities are then written as[10, 11)]

$$R_s = \left|r_s\right|^2 = \left|\frac{\cos\theta - \sqrt{\varepsilon_{(1)} - \sin^2\theta}}{\cos\theta + \sqrt{\varepsilon_{(1)} - \sin^2\theta}}\right|^2 \tag{1}$$

for *s*-polarization, and as

$$R_p = \left|r_p\right|^2 = \left|\frac{\sqrt{\varepsilon_{(2)}\varepsilon_{(3)}}\cos\theta - \sqrt{\varepsilon_{(3)} - \sin^2\theta}}{\sqrt{\varepsilon_{(2)}\varepsilon_{(3)}}\cos\theta + \sqrt{\varepsilon_{(3)} - \sin^2\theta}}\right|^2 \tag{2}$$

for *p*-polarization.

Here, we deal with cubic and uniaxial diatomic compounds whose primitive cell contains only one formula unit. In those materials, $\varepsilon_{(j)}$ may be expressed as either $\varepsilon_{\parallel}(\omega)$ or $\varepsilon_{\perp}(\omega)$ of [12)]

$$\varepsilon_{\parallel,\perp}(\omega) = \varepsilon_{\infty\parallel,\perp} \frac{(\omega_{\mathrm{LO}\parallel,\perp}/\omega_0)^2 - (\omega/\omega_0)^2 - i\gamma_{\mathrm{LO}\parallel,\perp}\omega/\omega_0^2}{(\omega_{\mathrm{TO}\parallel,\perp}/\omega_0)^2 - (\omega/\omega_0)^2 - i\gamma_{\mathrm{TO}\parallel,\perp}\omega/\omega_0^2} \quad , \tag{3}$$

where $\omega_{\mathrm{LO}\parallel,\perp}$ and $\omega_{\mathrm{TO}\parallel,\perp}$ are the resonance frequencies of LO and TO modes, and the suffixes $\parallel$ and $\perp$ signify the polarization directions, being parallel and perpendicular to the *c*-axis, respectively: $\gamma_{\mathrm{LO}\parallel,\perp}$ and $\gamma_{\mathrm{TO}\parallel,\perp}$ are the damping energies of LO and TO modes, respectively, whereas $\varepsilon_{\infty\parallel,\perp}$ denotes the infrared dielectric constant and ω_0 is the center of gravity of the frequencies of TO modes, that is, $(2\omega_{\mathrm{TO}\perp} + \omega_{\mathrm{TO}\parallel})/3$. In cubic materials, all the quantities for the direction $\parallel c$ are equal to the quantities for the direction $\perp c$, and ω_0 is identical with ω_{TO}.

We choose the three model compounds listed in Table I. Figure 2 shows the TO–LO regions of the three model compounds. The first one is a standard compound of group II–VI and III–V cubic semiconductors. The second one is GaN, which is chosen as a representative of materials having the wurtzite structure in which the TO–LO band is split into components $\parallel c$ and $\perp c$, but the two split-off bands overlap. Layered h-BN is chosen as the third model compound in view of the fact that its split-off bands are completely isolated [13, 14)].

2.1 TO and LO modes with no damping

To begin with, we calculate the spectrum by choosing $\theta = 10°$ as a typical example of the angle of incidence. In addition, to look into the basic properties of crystal optics, we treat TO and LO modes with no damping.

2.1.1 Cubic crystal

According to eqs. (1) and (2), the reflectivities of a cubic crystal are simply given by

$$R_s = \left| \frac{\cos\theta - \sqrt{\varepsilon(\omega) - \sin^2\theta}}{\cos\theta + \sqrt{\varepsilon(\omega) - \sin^2\theta}} \right|^2 \tag{4a}$$

and

$$R_p = \left| \frac{\varepsilon(\omega)\cos\theta - \sqrt{\varepsilon(\omega) - \sin^2\theta}}{\varepsilon(\omega)\cos\theta + \sqrt{\varepsilon(\omega) - \sin^2\theta}} \right|^2 . \qquad (4b)$$

When $\theta = 0°$, the total reflection due to negative ε spans in the interval $\omega_{TO} \le \omega \le \omega_{LO}$, making a reststrahlen band. Figure 3 shows how R_s and R_p change from the normal-incidence reflectivity R_n upon raising θ to 10°. As shown in Fig. 3, the changes are not much significant around the TO edge, but Snell's law gives rise to additional total reflection at frequencies above the LO edge of the reststrahlen band in the range given by

$$0 \le \varepsilon(\omega) \le \sin^2\theta . \qquad (5)$$

To distinguish it from the total reflection of the original reststrahlen band, we hereafter refer to the additional total reflection as Snell's total reflection (STR), denoting the edge of STR as S. Combining eq. (3) with eq. (5) with $\gamma_{LO\parallel,\perp} = \gamma_{TO\parallel,\perp} = 0$, and omitting the suffixes $\parallel$ and $\perp$, we obtain the frequency of S:

$$\omega_S^2 = \omega_{LO}^2 + \frac{(\omega_{LO}^2 - \omega_{TO}^2)\sin^2\theta}{\varepsilon_\infty - \sin^2\theta} . \qquad (6)$$

As ω increases further beyond ω_S, R_s decreases towards the well-known antiresonance at $\omega = \omega_p$ of

$$\omega_p^2 = \frac{\varepsilon_\infty \omega_{LO}^2 - \omega_{TO}^2}{\varepsilon_\infty - 1} \qquad (7)$$

due to the lattice plasma wave, which gives $\varepsilon(\omega_p) = 1$ in the absence of damping.

In contrast, for *p*-polarization, before reaching the lattice-plasma antiresonance, R_p drops to 0 at a frequency satisfying

$$\varepsilon(\omega) = \tan^2\theta . \qquad (8)$$

This is Brewster's null reflection (hereafter referred to as BNR) mentioned in §1. The null-reflection point B of the spectrum takes place at $\omega = \omega_B$ of

$$\omega_B^2 = \omega_{LO}^2 + \frac{(\omega_{LO}^2 - \omega_{TO}^2)\tan^2\theta}{\varepsilon_\infty - \tan^2\theta} . \qquad (9)$$

Indeed, as shown in Fig. 3, R_p abruptly drops from 100% to 0% as ω goes from ω_S through ω_B. As ω increases further from ω_B, R_p returns quickly to the values of its inherent lattice-plasma reflection. In short, since $\varepsilon(\omega)$ is positive but is much smaller than unity at frequencies just above a LO mode, Brewster's law, as well as Snell's law, holds at such a small angle of incidence as 10°, exerting a pronounced effect on the reflection spectrum.

2.1.2 Uniaxial crystals

As seen in Fig. 1, experimental configurations for anisotropic crystals are specified by the polarization *s* or *p*, the direction x_2 of the plane of incidence, and the crystal face, that is, the x_3-face. In a uniaxial crystal there are six principal configurations. Here, we write the principal configurations as sx_2x_3 or px_2x_3, expressing x_2 and x_3 in terms of the crystal axes *a* and *c*. From eqs. (1) and (2), the reflectivities in the six principal configurations are given as follows:

(1) configurations *sac* and *pac* with arbitrary plane of incidence on *c*-face,

$$R_{sac} = \left| \frac{\cos\theta - \sqrt{\varepsilon_\perp(\omega) - \sin^2\theta}}{\cos\theta + \sqrt{\varepsilon_\perp(\omega) - \sin^2\theta}} \right|^2 \tag{10a}$$

and

$$R_{pac} = \left| \frac{\sqrt{\varepsilon_\parallel(\omega)\varepsilon_\perp(\omega)}\cos\theta - \sqrt{\varepsilon_\parallel(\omega) - \sin^2\theta}}{\sqrt{\varepsilon_\parallel(\omega)\varepsilon_\perp(\omega)}\cos\theta + \sqrt{\varepsilon_\parallel(\omega) - \sin^2\theta}} \right|^2 ; \tag{10b}$$

(2) configurations *saa* and *paa* with plane of incidence $\perp$ *c*-axis on *a*-face,

$$R_{saa} = \left| \frac{\cos\theta - \sqrt{\varepsilon_\parallel(\omega) - \sin^2\theta}}{\cos\theta + \sqrt{\varepsilon_\parallel(\omega) - \sin^2\theta}} \right|^2 \tag{11a}$$

and

$$R_{paa} = \left| \frac{\varepsilon_\perp(\omega)\cos\theta - \sqrt{\varepsilon_\perp(\omega) - \sin^2\theta}}{\varepsilon_\perp(\omega)\cos\theta + \sqrt{\varepsilon_\perp(\omega) - \sin^2\theta}} \right|^2 ; \tag{11b}$$

(3) configurations *sca* and *pca* with plane of incidence ||*c*-axis on *a*-face,

$$R_{sca} = \left| \frac{\cos\theta - \sqrt{\varepsilon_{\perp}(\omega) - \sin^2\theta}}{\cos\theta + \sqrt{\varepsilon_{\perp}(\omega) - \sin^2\theta}} \right|^2 \tag{12a}$$

and

$$R_{pca} = \left| \frac{\sqrt{\varepsilon_{\parallel}(\omega)\varepsilon_{\perp}(\omega)}\cos\theta - \sqrt{\varepsilon_{\perp}(\omega) - \sin^2\theta}}{\sqrt{\varepsilon_{\parallel}(\omega)\varepsilon_{\perp}(\omega)}\cos\theta + \sqrt{\varepsilon_{\perp}(\omega) - \sin^2\theta}} \right|^2 . \tag{12b}$$

We note from these expressions that STR arises in the configurations *sac*, *saa*, *paa*, and *sca* when

$$\varepsilon_{\parallel}(\omega) \le \sin^2\theta, \text{ or } \varepsilon_{\perp}(\omega) \le \sin^2\theta, \tag{13a}$$

in *pac* when

$$\varepsilon_{\parallel}(\omega) \lesseqgtr \sin^2\theta \quad \text{for} \quad \varepsilon_{\parallel}(\omega)\varepsilon_{\perp}(\omega) \gtreqless 0 , \tag{13b}$$

and in *pca* when

$$\varepsilon_{\perp}(\omega) \lesseqgtr \sin^2\theta \quad \text{for} \quad \varepsilon_{\parallel}(\omega)\varepsilon_{\perp}(\omega) \gtreqless 0 . \tag{13c}$$

We then obtain

$$\omega^2_{S\parallel,\perp} = \omega^2_{LO\parallel,\perp} + \frac{(\omega^2_{LO\parallel,\perp} - \omega^2_{TO\parallel,\perp})\sin^2\theta}{\varepsilon_{\infty\parallel,\perp} - \sin^2\theta} \tag{14}$$

for the frequencies of the upper or lower bound, $S_{\parallel}$ and $S_{\perp}$, of the STRs.

It is evident from eqs. (10b), (11b), and (12b) that the frequencies of BNR are the ones of two solutions of the following equations:

$$\varepsilon^2_{\perp}(\omega)\cos^2\theta = \varepsilon_{\perp}(\omega) - \sin^2\theta \tag{15a}$$

in *paa*,

$$\varepsilon_{\parallel}(\omega)\varepsilon_{\perp}(\omega)\cos^2\theta = \varepsilon_{\parallel}(\omega) - \sin^2\theta \tag{15b}$$

in *pac*, and

$$\varepsilon_{\parallel}(\omega)\varepsilon_{\perp}(\omega)\cos^2\theta = \varepsilon_{\perp}(\omega) - \sin^2\theta \qquad (15c)$$

in *pca*. Concerning eq. (15a), we obtain the solution

$$\varepsilon_{\perp}(\omega) = \tan^2\theta\,, \qquad (16)$$

which gives the frequency of BNR, $\omega_{\mathrm{B}paa}$, in the configuration *paa*:

$$\omega_{\mathrm{B}paa}^2 = \omega_{\mathrm{LO}\perp}^2 + \frac{(\omega_{\mathrm{LO}\perp}^2 - \omega_{\mathrm{TO}\perp}^2)\tan^2\theta}{\varepsilon_{\infty\perp} - \tan^2\theta}\,. \qquad (17)$$

The other solution

$$\varepsilon_{\perp}(\omega) = 1 \qquad (18)$$

of eq. (15a) gives the lattice-plasma antiresonance for the polarization $\perp c$. In the configuration *paa* the infrared beam is the ordinary ray, so that the frequency of the antiresonance is independent of θ. However, since the infrared beams are extraordinary rays in the configurations *pac* and *pca*, the frequencies of both the BNR and lattice-plasma antiresonance given by eqs. (15b) and (15c) depend on θ.

(a) *GaN-type crystal*

Figure 4 shows the spectra for the six principal configurations in the frequency region of the LO modes of the crystal of GaN-type compound. For *s*-polarization, STR occurs for all configurations. In accord with the direction of the electric field vector of the incident light, the total reflection extends from the edge at $\mathrm{LO}_{\perp}$ up to $\mathrm{S}_{\perp}$ in *sac* and *sca*, and from the edge at $\mathrm{LO}_{\parallel}$ up to $\mathrm{S}_{\parallel}$ in *saa*. For *p*-polarization, on the other hand, STR occurs at the $\mathrm{LO}_{\parallel}$ edge in *pac* and at the $\mathrm{LO}_{\perp}$ edge in *paa* and *pca*, as shown in Fig. 4.

As for BNR, since $\omega_{\mathrm{LO}\parallel} < \omega_{\mathrm{LO}\perp}$ in the model GaN-type crystal, $\varepsilon_{\perp}$ remains to be negative around $\mathrm{LO}_{\parallel}$, while $\varepsilon_{\parallel}$ varies through zero at $\omega_{\mathrm{LO}\parallel}$. Thus, from eq. (15b), BNR in the configuration *pac* occurs just above $\mathrm{LO}_{\parallel}$. R_{pac} recovers quickly from BNR to the total reflection at $\mathrm{S}_{\parallel}$ and it lasts up to $\mathrm{LO}_{\perp}$. To see how B_{pac} and $\mathrm{S}_{\parallel}$ vary with θ we have examined the solution of eq. (15b) and $\omega_{\mathrm{S}\parallel}$ of eq. (14) for $\theta > 10°$. It turns out that as θ increases, B_{pac} and $\mathrm{S}_{\parallel}$ shift toward higher frequencies: When θ reaches θ_0 satisfying the relation

$$\sin^2\theta_0 = \varepsilon_{\parallel}(\omega_{\mathrm{LO}\perp})\,, \qquad (19)$$

B_{pac} and $S_{\parallel}$ coincide with $LO_{\perp}$. In the case of the present model crystal, we have $\theta_0 = 29.7°$. Upon further increase in θ, B_{pac} shifts toward higher frequencies faster than $S_{\parallel}$ and approaches the lattice-plasma antiresonance frequency $\omega_{p\parallel}$ of $1.398\omega_0$. A similar situation at $\theta = 70°$ in 6H-SiC has been shown by Tiwald et al.,[15] who have discussed STR in relation to spectroscopic ellipsometry.

In the configuration *paa*, since the infrared light is the ordinary ray as in the case of cubic crystals, STR extends to $S_{\perp}$ as shown in Fig. 4(b). It accompanies BNR at ω_{Bpaa} given by eq. (17).

In the configuration *pca*, the total reflection due to the component $\parallel c$ of the electric field of light ceases once at the frequency of $LO_{\parallel}$ but the component $\perp c$ of the electric field of light causes the recovery of the total reflection in the frequency region between $LO_{\perp}$ and $S_{\perp}$. Because of the extraordinary character of this light, BNR occurs just above $S_{\perp}$.

(b) *h-BN-type crystal*

Figure 5 shows the spectra around LO modes of the model crystal of the h-BN-type compound. In accord with the results observed in the GaN-type crystal, the total reflection is seen in all configurations of *s*-polarization, and besides, R_{pac} and R_{paa} each exhibit the same behaviors as R_{pac} and R_{paa} of the GaN-type crystal at the edge of $LO_{\perp}$. There are, however, striking differences in other aspects. This is because, in contrast to the case of GaN-type crystal, the $(TO–LO)_{\parallel}$ band is completely separated in frequency from the $(TO–LO)_{\perp}$ band in the h-BN-type crystal. In other words, in the frequency region of the $(TO–LO)_{\parallel}$ band, we have $\varepsilon_{\parallel} \le 0 < \varepsilon_{\perp}$, whereas, in the frequency region of the $(TO–LO)_{\perp}$ band, the inequality relationship is reversed such that $\varepsilon_{\perp} \le 0 < \varepsilon_{\parallel}$. As a result, BNRs in the configurations *pac* and *pca* take place below $LO_{\parallel}$ and $LO_{\perp}$, respectively, as shown in Figs. 5(a) and 5(c).

2.2 Effect of damping

Now, we proceed to a realistic quantitative calculation of reflectivity by introducing nonvanishing damping constants of the optical modes into the dielectric functions. In this study, we choose $\gamma_{LO\parallel,\perp} = \gamma_{TO\parallel,\perp} = 2\times10^{-3}\omega_0$ for all three model crystals.

2.2.1 Cubic crystal

Figure 6 shows the whole spectra of *s*- and *p*-polarizations at $\theta = 10°$ in the model cubic compound. There appears a typical reststrahlen band with the lattice-plasma antiresonance

given by eq. (7) at $1.35\omega_0$. Although BNR is strongly suppressed by damping, a close look at the LO edge, shown in the inset of Fig. 6, leads us to identify the specific behaviors of the *s*- and *p*-spectra shown in Fig. 3. The difference between *s*- and *p*-polarizations is demonstrated by a marked dip due to BNR in the spectrum of $R_p - R_s$, as shown in Fig. 7, where the variation in $R_p - R_s$ with the change in θ from 5 to 15° is shown. We note that the dip becomes deep enough to be experimentally detected if θ is raised to about 10°.

2.2.2 Uniaxial crystals

Figure 8 shows the calculated spectra of the GaN-type model crystal for six configurations at $\theta = 10°$. BNR is observed as a striking dip in R_{pac} in Fig. 8(a). The fine structure in R_{pca} in Fig. 8(c) is also related to BNR. Again, the dip and fine structure are suppressed extremely by damping. However, the complete feature of the effect of BNR and STR is revealed if we plot $R_{pac} - R_{sac}$, $R_{paa} - R_{sca}$, and $R_{pca} - R_{saa}$, as shown in Fig. 9. All the minima and maxima arise from either BNR or STR associated with $LO_{\parallel}$ and $LO_{\perp}$.

Figure 10 shows the spectra covering two reststrahlen bands of h-BN at $\theta = 10°$. Figure 11 shows the difference spectra of $R_{pac} - R_{sac}$, $R_{paa} - R_{sca}$, and $R_{pca} - R_{saa}$ at $\theta = 5$, 10, and 15°. The structures of BNR and STR manifest themselves clearly in Fig. 11. Since the breadth of $(TO-LO)_{\perp}$ is about 5 times as large as the breadth of $(TO-LO)_{\parallel}$, the structures of BNR and STR associated with $LO_{\perp}$ are significantly larger than the structures associated with $LO_{\parallel}$. The reflectivity differences associated with $LO_{\perp}$ are found to exceed 10% already at $\theta = 5°$.

3. Discussion

The dip in R_{pac} of a GaN crystal has appeared in the spectrum calculated by Barker and Ilegems for $\theta = 50°$.[16] It has been verified experimentally by Kuroda et al.[17] The observation of a doublet structure at $\theta = 10°$ has permitted Kuroda et al. to precisely determine the resonance frequencies of $LO_{\parallel}$ and $LO_{\perp}$ of a 35-μm-thick crystal grown by hydride vapor phase epitaxy (HVPE). The spectra in calcite treated by Decius et al.[3] correspond to the R_{pac} and R_{pca} of the h-BN-type crystal around $LO_{\parallel}$ and $LO_{\perp}$, respectively. It is now evident from the present study that these remarkable spectral features arise universally from the combined effect of BNR and STR in uniaxial polar crystals.

We note from Figs. 7, 9, and 11 that all the features of the difference spectrum are intensified as θ is elevated, and that the differences in reflectivity reach or exceed ±10% at $\theta = 10°$. At the same time, except for the BNR structures B_{pac} and B_{pca} of the h-BN-type

crystal, these features shift toward higher frequencies. Figure 12 shows the variations with θ of the frequencies of B of the cubic model crystal, B_{pac} and $S_{\perp}$ of the GaN-type model crystal, and B_{pac}, $S_{\parallel}$, and $S_{\perp}$ of the h-BN-type model crystal, which are obtained in the absence of damping. As long as $\theta \lesssim 20°$, these frequencies show a quadratic variation with θ and agree well with positions of the corresponding minima and maxima appearing in the difference spectra in Figs. 7, 9, and 11. The coefficients of the shifts are found to be smaller than $2\times10^5\omega_0$ deg^{-2}. In a number of ionic crystals and compound semiconductors, we have $\omega_0 \lesssim 500$ cm^{-1}.[18] Present calculation ensures the shift to be smaller than 1 cm^{-1}, being comparable to the standard spectral resolution of an FTIR spectrometer, at $\theta = 10°$ in such ionic crystals and compound semiconductors.

4. Conclusions

The total reflection due to Snell's law and the null reflection due to Brewster's law have been put to various practical uses in photonics of materials. Such uses employ an angle of incidence greater than 45° since the refractive index $\sqrt{\varepsilon(\omega)}$ is greater than unity at frequencies of relevant light. The present study has focused for the first time on the fact that, at frequencies just above the LO mode of infrared lattice vibration, the refractive index may be much smaller than unity, and thus the total reflection and null reflection may take place at angles of incidence much smaller than 45°. A model approach to the oblique-incidence infrared reflection spectrum in cubic and uniaxial crystals has been performed numerically for all the principal configurations of the crystal face, the plane of incidence, and the polarization of light. The results show that an angle of incidence of approximately 10° is sufficiently large to produce steep and observable line structures due to LO phonons in the spectrum of the *s*- and *p*-polarizations. It has long been conceived that, in a thick crystal of polar materials, it is difficult to observe the first-order excitation of TO and LO phonons separately by infrared spectroscopy. However, small-angle oblique-incidence reflectometry overcomes this difficulty and provides reliable, quantitative information on the properties of these phonons.

1) M. Born and E. Wolf: *Principles of Optics* (Pergamon Press, New York, 1974) 5th ed., Chap. 1.
2) L. P. Mosteller, Jr. and F. Wooten: J. Opt. Soc. Am. **58** (1968) 511.
3) J. C. Decius, R. Frech, and P. Brüesch: J. Chem. Phys. **58** (1973) 4056.
4) O. E. Piro: Phys. Rev. B **36** (1987) 3427.
5) D. W. Berreman: Phys. Rev. **130** (1963) 2193.
6) M. D. Sciacca, A. D. Mayur, E. Oh, A. K. Ramdas, S. Rodriguez, J. K. Furdyna, M. R. Melloch, C. P. Beetz, and W. S. Yoo: Phys. Rev. B **51** (1995) 7744.
7) T. Ito, T. Kawashima, H. Yamaguchi, T. Masumi, and S. Adachi: J. Phys. Soc. Jpn. **67** (1998) 2125.
8) J. N. Hilfiker, C. L. Bungay, R. A. Synowicki, T. E. Tiwald, C. M. Herzinger, B. Johs, G. K. Pribil, and J. A. Woollam: J. Vac. Sci. Technol. A **21**(4) (2003) 1103, and the references therein.
9) Y. Kumagai, T. Himoto, H. Yokoi, H. Tampo, and N. Kuroda: Abstr. Meet. Tohoku Chap. Japan Society of Applied Physics (63rd Annu. Meet., 2008), p. 105, 4aB11 [in Japanese].
10) P. Brüesch: *Phonons*: *Theory and Experiments II* (Springer–Verlag, Berlin, 1986) Appendix B.4.
11) M. Schubert, T. E. Tiwald, and C. M. Herzinger: Phys. Rev. B **61** (2000) 8187.
12) F. Gervais and B. Piriou: J. Phys. C: Solid State Phys. **7** (1974) 2374.
13) R. Geick, C. H. Perry, and G. Rupprecht: Phys. Rev. **146** (1966) 543.
14) M. Schubert, E. Franke, H. Neumann, T. E. Tiwald, D. W. Thompson, J. A. Woollam, and J. Hahn: Thin Solid Films **313-314** (1998) 692.
15) T. E. Tiwald, J. A. Woollam, S. Zollner, J. Christiansen, R. B. Gregory, T. Wetteroth, and S. R. Wilson: Phys. Rev. B **60** (1999) 11464.
16) A. S. Barker, Jr. and M. Ilegems: Phys. Rev. B **7** (1973) 743.
17) N. Kuroda, T. Kitayama, Y. Nishi, K. Saiki, H. Yokoi, J. Watanabe, M. W. Cho, T. Egawa, and H. Ishikawa: Jpn. J. Appl. Phys. **45** (2006) 646.
18) P. Brüesch: *Phonons*: *Theory and Experiments II* (Springer–Verlag, Berlin, 1986) Chap. 2.

Fig. 1 Optical configuration for the measurement of oblique-incidence reflectivity. $\boldsymbol{E}_s$ and $\boldsymbol{E}_p$ denote the *s*- and *p*-polarized electric field of light, respectively.

Fig. 2 Frequency regions between TO and LO modes of three model crystals treated in the present work. Suffices || and ⊥ signify the directions of polarization parallel and perpendicular to the *c*-axis, respectively.

Fig. 3 Reflectivity spectra of the cubic model crystal with no damping for three configurations: normal-incidence reflectivity R_{n} (dotted line), oblique-incidence reflectivity R_s for *s*-polarization at θ = 10° (dash-dotted line) and oblique-incidence reflectivity R_p for *p*-polarization at θ = 10° (solid line).

Fig. 4 Reflectivity spectra of the GaN-type model crystal with no damping for *s*- and *p*-polarizations at θ = 10°: (a) R_{sac} (dash-dotted line) and R_{pac} (solid line), (b) R_{saa} (dash-dotted line) and R_{paa} (solid line), and (c) R_{sca} (dash-dotted line) and R_{pca} (solid line).

Fig. 5 Reflectivity spectra of the h-BN-type model crystal with no damping for *s*- and *p*-polarizations at θ = 10°: (a) R_{sac} (dash-dotted line) and R_{pac} (solid line), (b) R_{saa} (dash-dotted line) and R_{paa} (solid line), and (c) R_{sca} (dash-dotted line) and R_{pca} (solid line).

Fig. 6 Reflectivity spectra of the h-BN-type model crystal with damping of $\gamma_{\mathrm{LO}\parallel,\perp} = \gamma_{\mathrm{TO}\parallel,\perp} = 2\times10^{-3}\omega_0$ for three configurations: normal-incidence reflectivity R_{n} (dotted line), oblique-incidence reflectivity R_s for *s*-polarization at θ = 10° (dash-dotted line) and oblique-incidence reflectivity R_p for *p*-polarization at θ = 10° (solid line). The inset shows an expansion around the frequency of LO mode.

Fig. 7 Variation of the difference spectrum $R_p - R_s$ of the cubic model crystal with θ.

Fig. 8 Reflectivity spectra of the GaN-type model crystal with a damping of $\gamma_{\mathrm{LO}\parallel,\perp} = \gamma_{\mathrm{TO}\parallel,\perp} = 2\times10^{-3}\omega_0$ for *s*- and *p*-polarizations at θ = 10°: (a) R_{sac} (dash-dotted line) and R_{pac} (solid line), (b) R_{saa} (dash-dotted line) and R_{paa} (solid line), and (c) R_{sca} (dash-dotted line) and R_{pca} (solid line).

Fig. 9 Variation of the difference spectrum, (a) $R_{pac} - R_{sac}$, (b) $R_{paa} - R_{sca}$, and (c) $R_{pca} - R_{saa}$, of

the GaN-type model crystal with a damping of $\gamma_{LO\parallel,\perp} = \gamma_{TO\parallel,\perp} = 2\times10^{-3}\omega_0$ with θ. BNR and STR show the origin of respective minimum and maximum.

Fig. 10 Reflectivity spectra of the h-BN-type model crystal with a damping of $\gamma_{LO\parallel,\perp} = \gamma_{TO\parallel,\perp} = 2\times10^{-3}\omega_0$ for *s*- and *p*-polarizations at $\theta = 10°$: (a) R_{sac} (dash-dotted line) and R_{pac} (solid line), (b) R_{saa} (dash-dotted line) and R_{paa} (solid line), and (c) R_{sca} (dash-dotted line) and R_{pca} (solid line).

Fig. 11 Variation of the difference spectrum, (a) R_{pac}–R_{sac}, (b) R_{paa}–R_{sca}, and (c) R_{pca}–R_{saa} , of h-BN-type model crystal with a damping of $\gamma_{LO\parallel,\perp} = \gamma_{TO\parallel,\perp} = 2\times10^{-3}\omega_0$ with θ. BNR and STR show the origin of respective minimum and maximum.

Fig. 12 Dependence on θ of the frequencies of (1) $S_\perp$ of GaN-type model crystal, (2) B_{pac} of GaN-type model crystal, (3) S of cubic model crystal, (4) $S_\perp$ of h-BN-type model crystal, (5) $S_\parallel$ of h-BN-type model crystal, and (6) B_{pac} of h-BN-type model crystal.

Table I. Normalized resonance energies of TO and LO modes and infrared dielectric constant of model materials used for numerical analysis.

material	direction of polarization	ω_{TO}/ω_0	ω_{LO}/ω_0	ε_∞
Cubic semiconductor	arbitrary	1.00	1.30	6.0
Wurtzite compound of GaN type	$\|c$	0.969	1.328	5.3
	$\perp c$	1.016	1.343	5.2
Layer compound of h-BN type	$\|c$	0.668	0.706	4.10
	$\perp c$	1.166	1.373	4.95

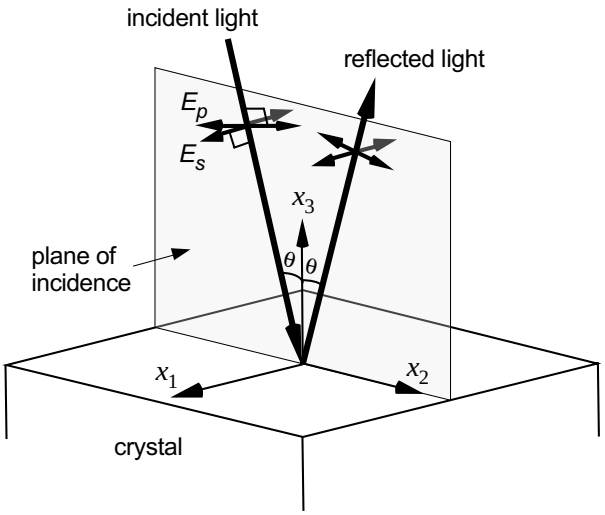
incident light
reflected light
E_p
E_s
x_3
plane of
incidence
θ
θ
x_1
x_2
crystal

Fig. 1

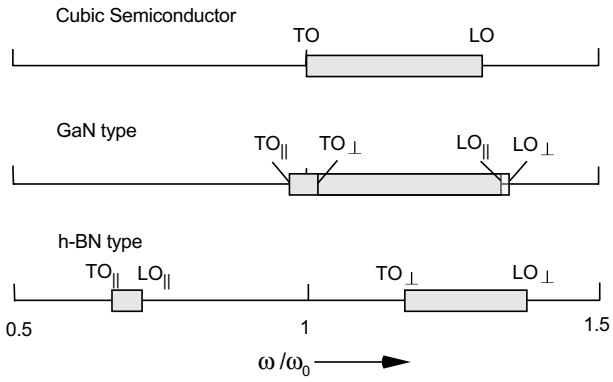
Cubic Semiconductor
TO
LO
GaN type
TO||
TO ⊥
LO||
LO ⊥
h-BN type
TO||
LO||
TO ⊥
LO ⊥
0.5
1
1.5
ω /ω0

Fig. 2

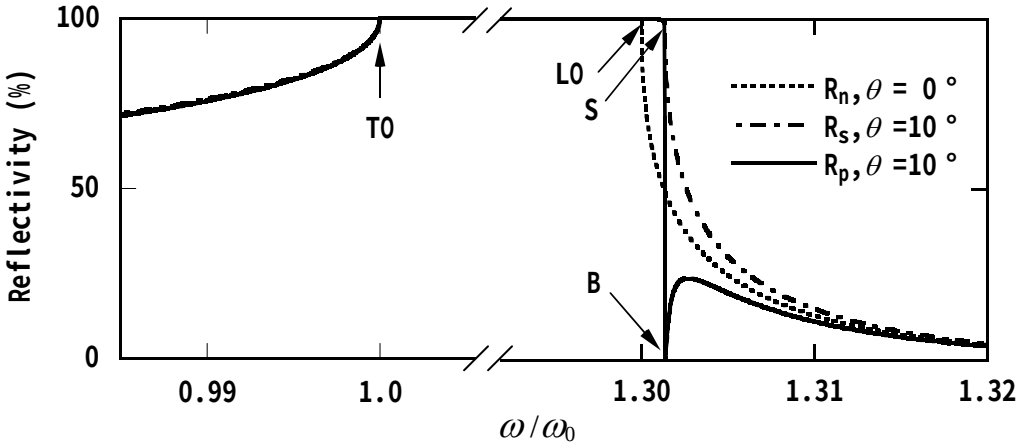
100
50
0
Reflectivity (%)
TO
LO
S
B
$R_n, \theta = 0°$
$R_s, \theta = 10°$
$R_p, \theta = 10°$
0.99
1.0
1.30
1.31
1.32
ω/ω_0

Fig. 3

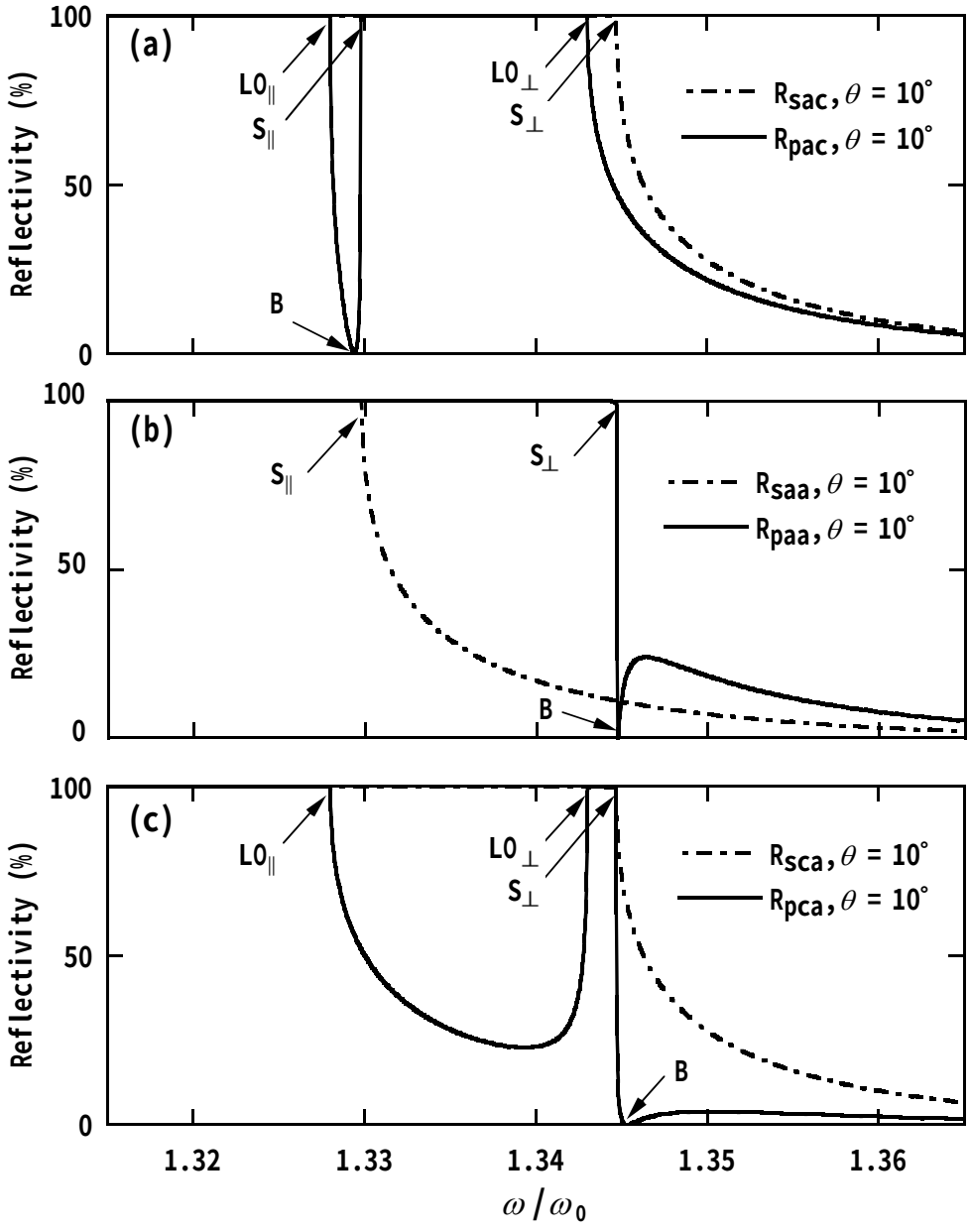
(a)
(b)
(c)
Reflectivity (%)
100
50
0
LO∥
S∥
LO⊥
S⊥
B
Rsac, θ = 10°
Rpac, θ = 10°
Rsaa, θ = 10°
Rpaa, θ = 10°
Rsca, θ = 10°
Rpca, θ = 10°
1.32
1.33
1.34
1.35
1.36
ω / ω0

Fig. 4

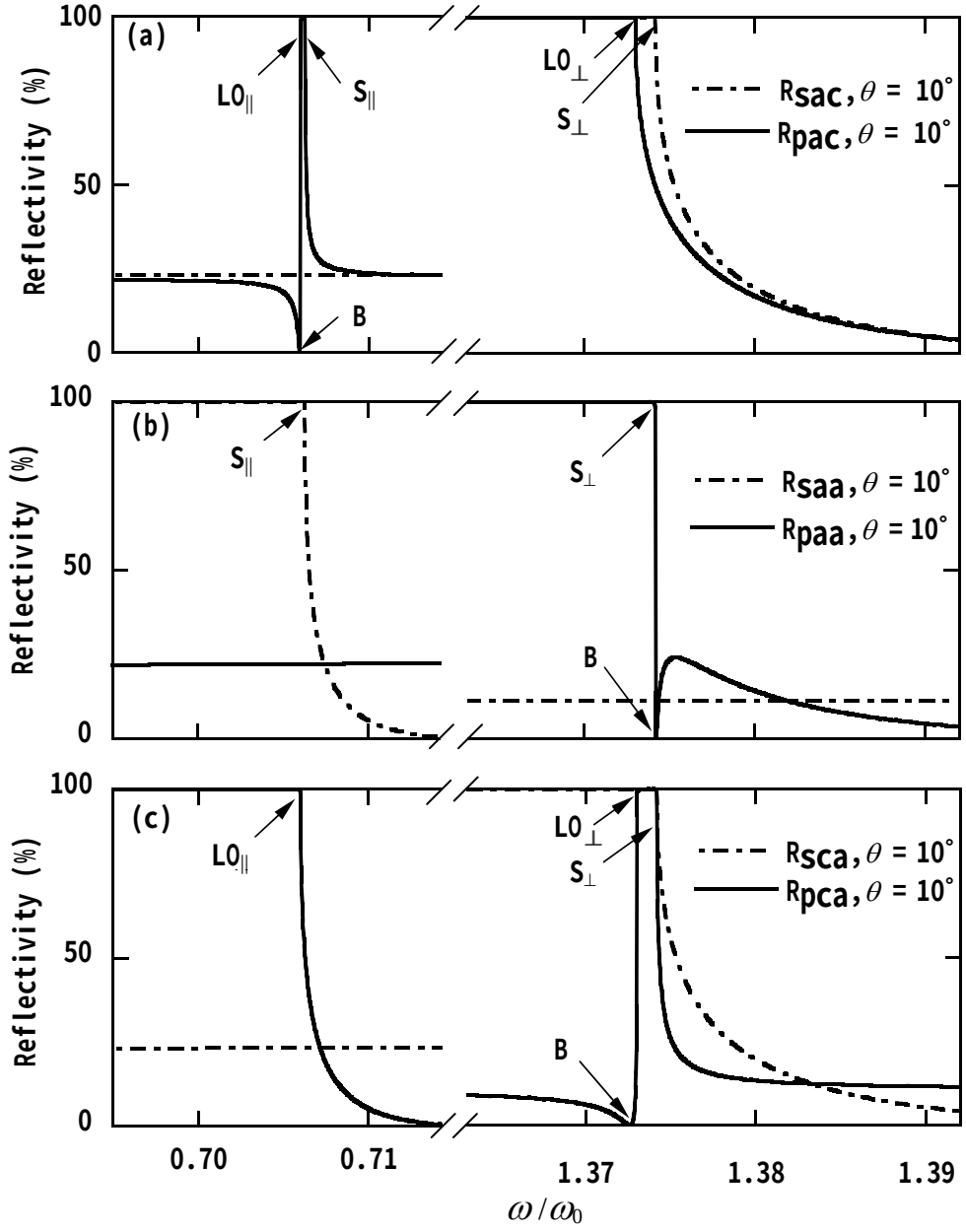
(a)
(b)
(c)
Reflectivity (%)
100
50
0
LO∥
S∥
LO⊥
S⊥
B
Rsac, θ = 10°
Rpac, θ = 10°
Rsaa, θ = 10°
Rpaa, θ = 10°
Rsca, θ = 10°
Rpca, θ = 10°
0.70
0.71
1.37
1.38
1.39
ω/ω0

Fig. 5

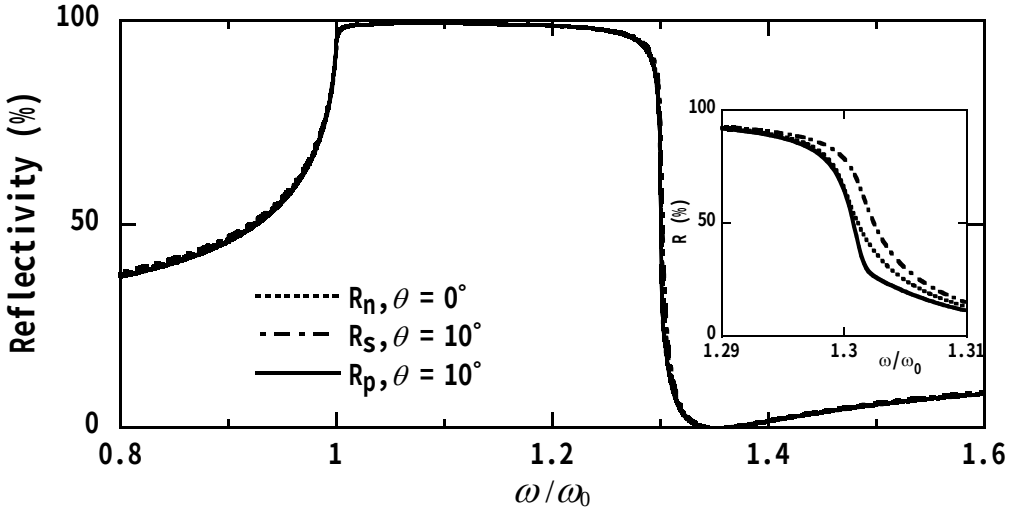
100
50
0
Reflectivity (%)
0.8
1
1.2
1.4
1.6
ω/ω_0
$R_n, \theta = 0°$
$R_s, \theta = 10°$
$R_p, \theta = 10°$
100
50
0
R (%)
1.29
1.3
1.31
ω/ω_0

Fig. 6

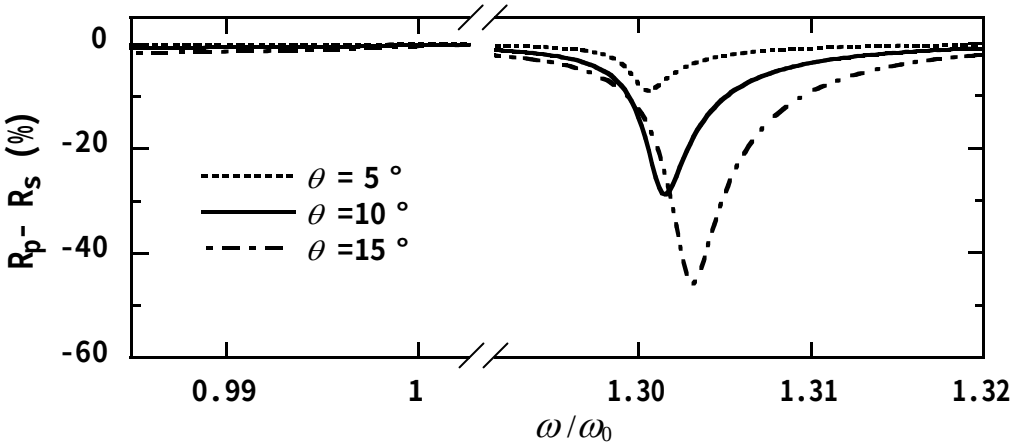
0
-20
-40
-60
$R_p - R_s$ (%)
θ = 5 °
θ =10 °
θ =15 °
0.99
1
1.30
1.31
1.32
ω/ω_0

Fig. 7

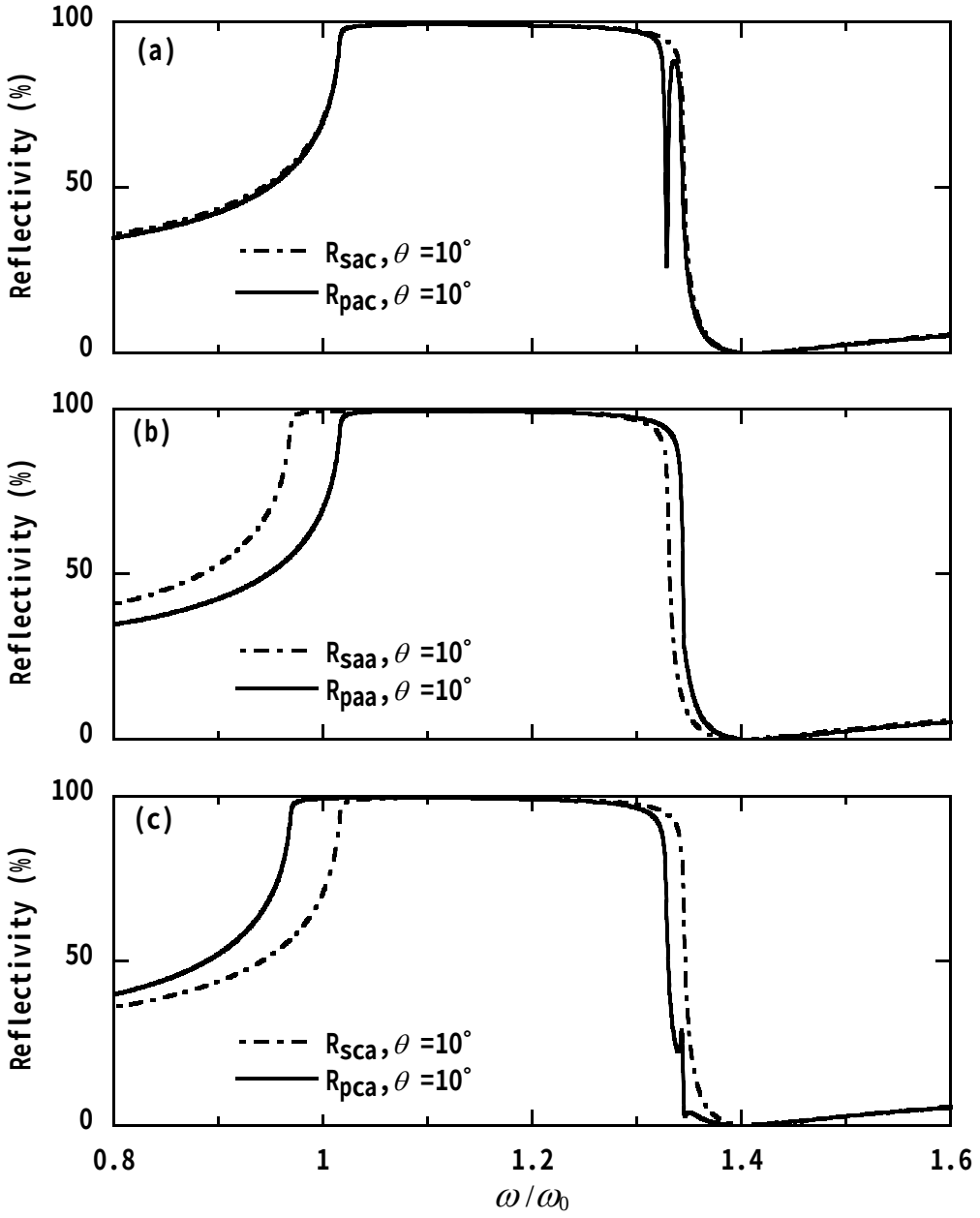
100
(a)
Reflectivity (%)
50
0
R_{sac}, θ =10°
R_{pac}, θ =10°
100
(b)
Reflectivity (%)
50
0
R_{saa}, θ =10°
R_{paa}, θ =10°
100
(c)
Reflectivity (%)
50
0
R_{sca}, θ =10°
R_{pca}, θ =10°
0.8
1
1.2
1.4
1.6
ω / ω_0

Fig.8

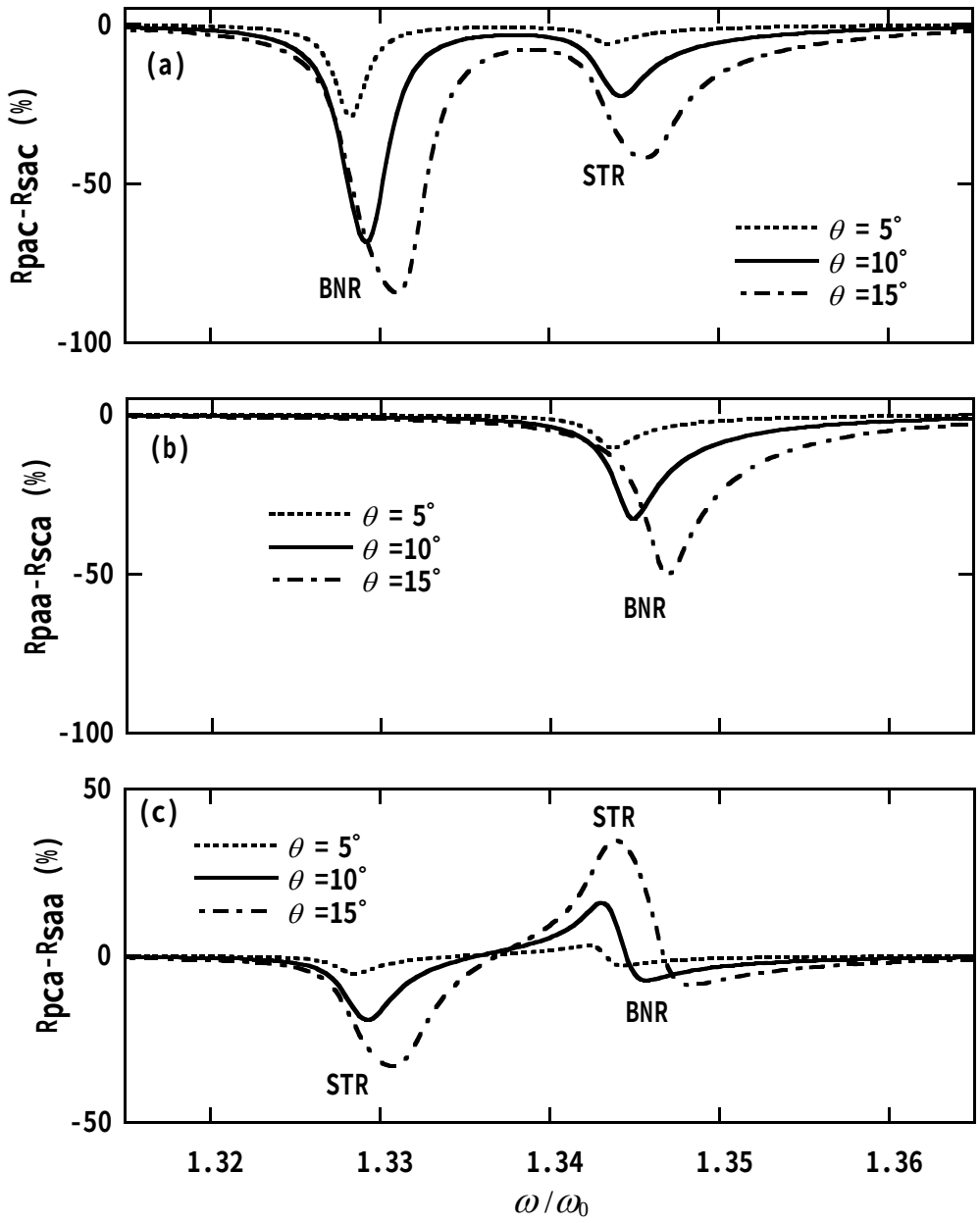
(a)
Rpac-Rsac (%)
0
-50
-100
BNR
STR
θ = 5°
θ =10°
θ =15°
(b)
Rpaa-Rsca (%)
0
-50
-100
θ = 5°
θ =10°
θ =15°
BNR
(c)
Rpca-Rsaa (%)
50
0
-50
θ = 5°
θ =10°
θ =15°
STR
BNR
STR
1.32
1.33
1.34
1.35
1.36
ω/ω0

Fig. 9

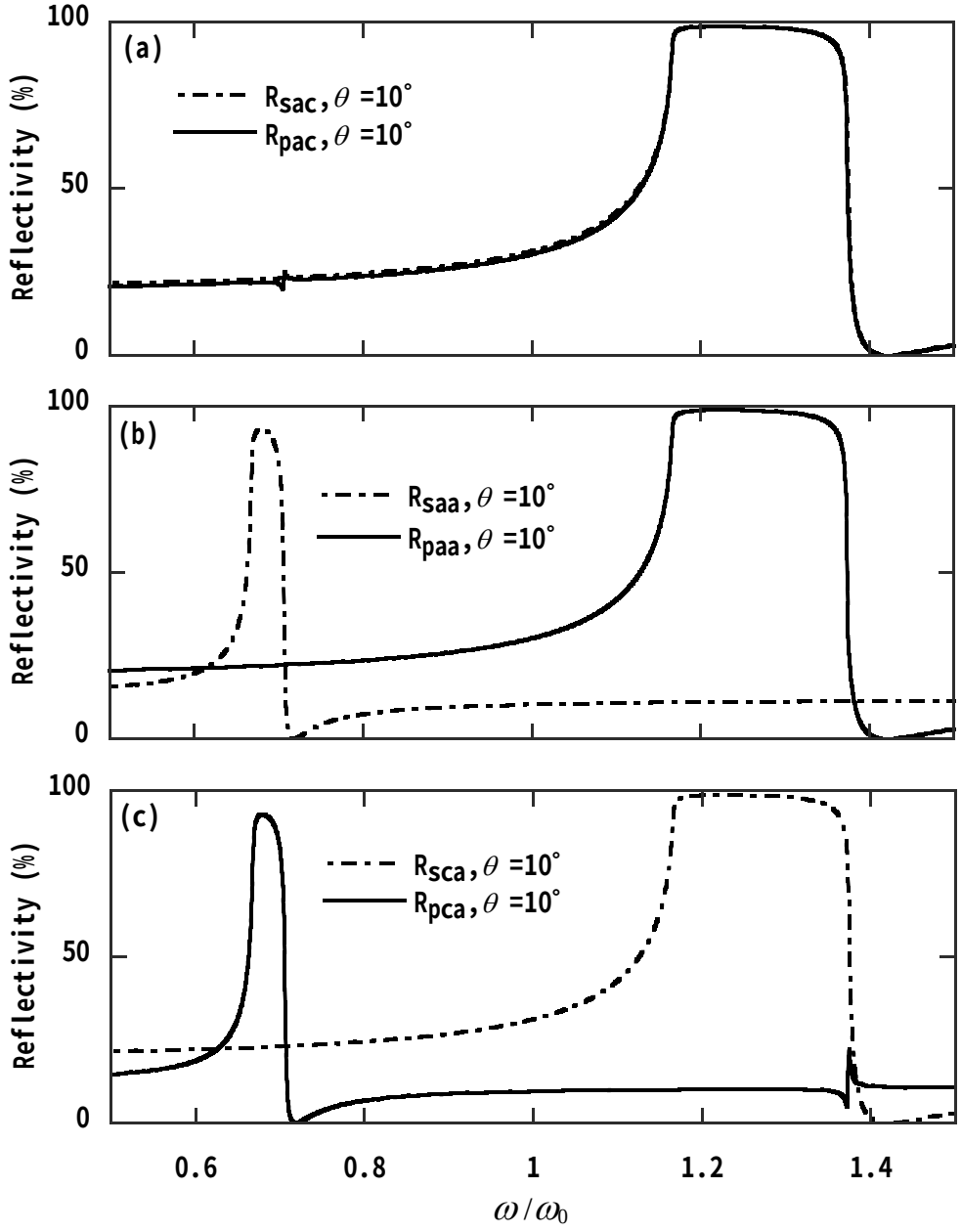
(a)
R_{sac}, θ =10°
R_{pac}, θ =10°
(b)
R_{saa}, θ =10°
R_{paa}, θ =10°
(c)
R_{sca}, θ =10°
R_{pca}, θ =10°
Reflectivity (%)
100
50
0
0.6
0.8
1
1.2
1.4
ω/ω_0

Fig. 10

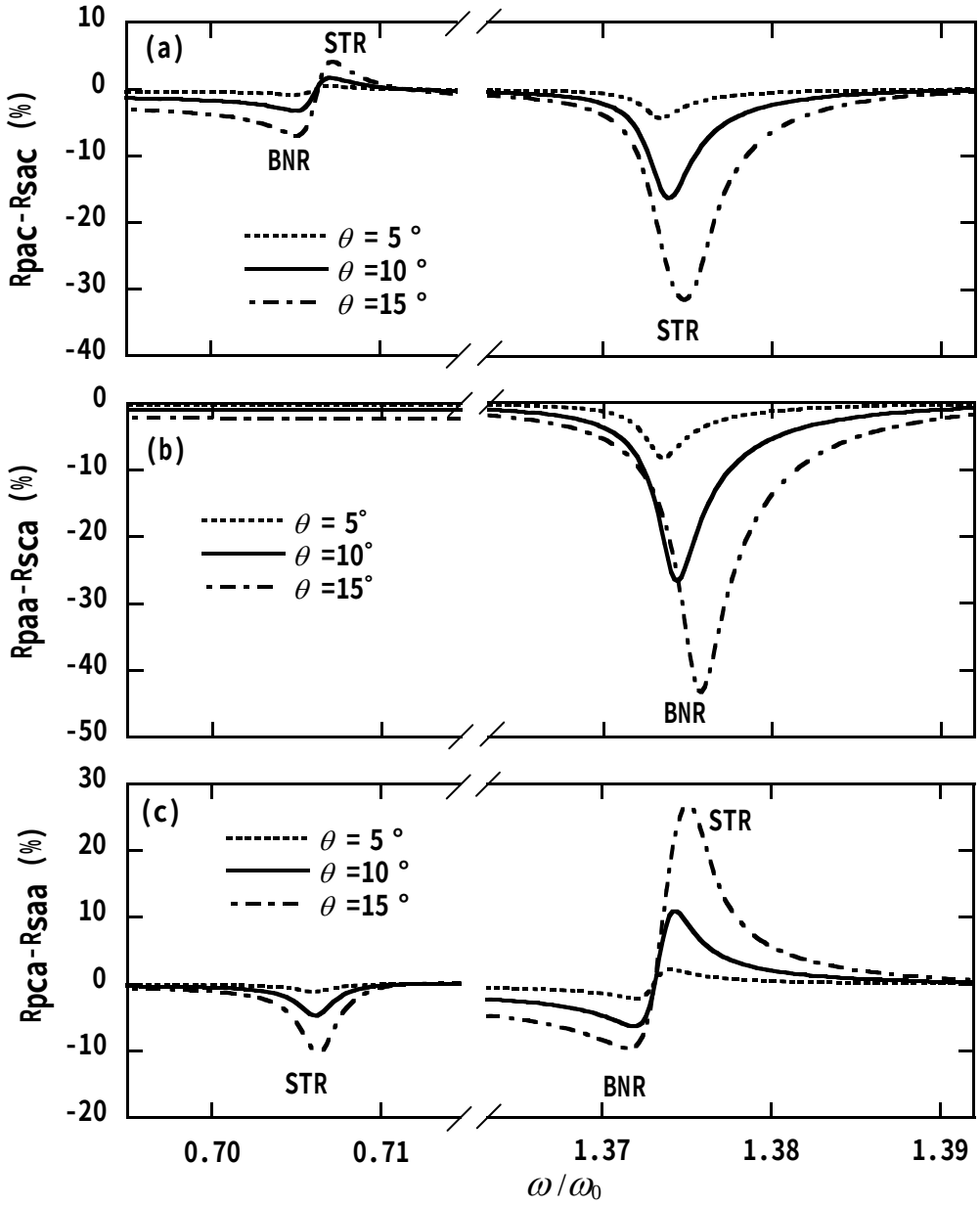
(a)
STR
BNR
θ = 5 °
θ =10 °
θ =15 °
STR
Rpac-Rsac (%)
(b)
θ = 5°
θ =10°
θ =15°
BNR
Rpaa-Rsca (%)
(c)
θ = 5 °
θ =10 °
θ =15 °
STR
STR
BNR
Rpca-Rsaa (%)
0.70
0.71
1.37
1.38
1.39
ω/ω0

Fig. 11

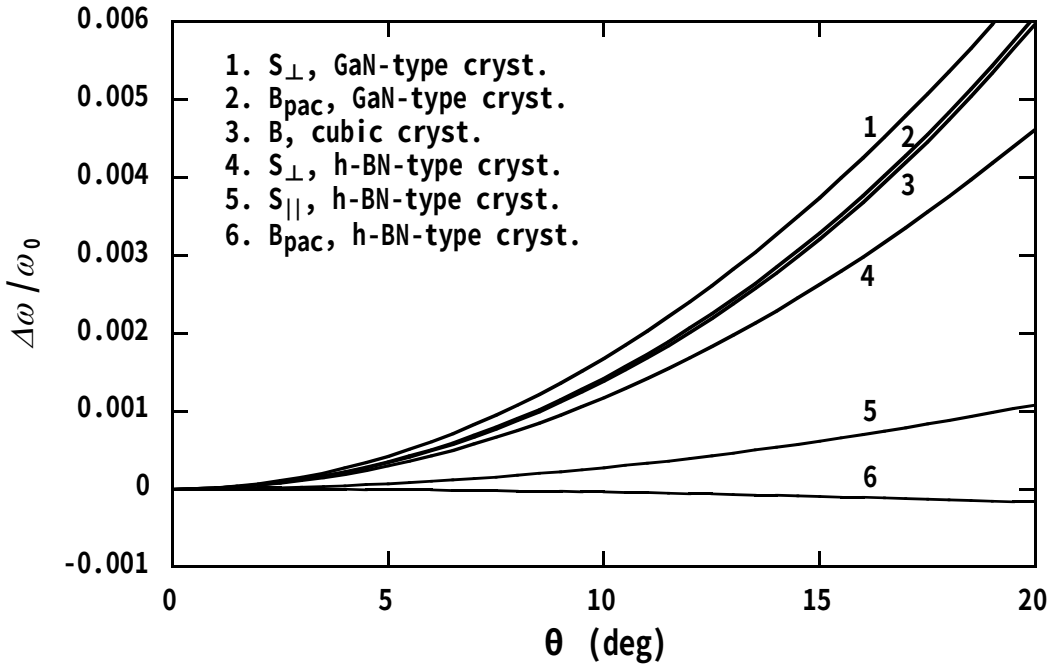
0.006
0.005
0.004
0.003
0.002
0.001
0
-0.001
0
5
10
15
20
θ (deg)
Δω / ω0
1. S⊥, GaN-type cryst.
2. Bpac, GaN-type cryst.
3. B, cubic cryst.
4. S⊥, h-BN-type cryst.
5. S||, h-BN-type cryst.
6. Bpac, h-BN-type cryst.
1
2
3
4
5
6

Fig. 12